remote sensing

MDPI

Article

Automated Inversion of Manning's Roughness and Flood Simulation in a One-Dimensional Hydrodynamic Model Constrained by SAR-Derived Inundation Extent: A Case Study of the Le'an River in Wuyuan

Siyu Wu [1,2], Zhiguo Pang [1,2,*], Daling Cao [1,2], Jun'e Fu [1,2], Wei Jiang [1,2] and Yao Zhao [1,2]

[1] State Key Laboratory of Simulation and Regulation of Water Cycle in River Basin, China Institute of Water Resources and Hydropower Research, Beijing 100038, China; wusiyu@edu.iwhr.com (S.W.); caodl@iwhr.com (D.C.); fuje@iwhr.com (J.F.); jiangwei@iwhr.com (W.J.); zhaoyao@edu.iwhr.com (Y.Z.)
[2] Innovation Center for Flood and Drought Disaster Reduction Technology, Ministry of Water Resources, Beijing 100038, China
* Correspondence: pangzg@iwhr.com

Highlights

What are the main findings?

- An automated SAR-constrained PSO framework was developed for spatially zoned Manning's roughness inversion in a one-dimensional HEC-RAS model, enabling direct coupling between 1D hydrodynamic outputs and 2D SAR inundation observations.
- The optimized Manning's roughness parameters improved inundation agreement (IoU: 0.763–0.789) and agreement with rating-curve-derived reference water levels (RMSE: 0.811–0.594 m; NSE: 0.950–0.973).

What are the implications of the main findings?

- Spatializing cross-sectional water-surface elevations enables SAR-derived inundation extent to directly constrain iterative parameter optimization in one-dimensional hydrodynamic models.
- The framework reduces reliance on dense and continuous gauge observations, providing a practical calibration approach for flood modeling in data-scarce small and medium-sized rivers.

Abstract

The difficulty in accurately determining channel Manning's roughness has long constrained the accuracy of river flood simulation. At present, Manning's roughness is mainly assigned using empirical approaches such as lookup tables and visual comparison, which are insufficient to represent the spatial heterogeneity of roughness in natural rivers. Remote sensing provides valuable data support for flood simulation in areas with sparse hydrological gauges. Remote-sensing observations are objective and can be acquired over large areas, but they are temporally discontinuous, whereas hydrodynamic models provide physically meaningful and temporally continuous simulations. These two information sources are therefore naturally complementary, providing a new avenue for Manning's roughness inversion through remote sensing and hydrodynamic model coupling. To address these challenges, this study proposes a new remote sensing and hydrodynamic model coupling framework centered on roughness inversion. SAR-derived inundation extent is used as a spatial constraint, and an objective function together with particle swarm optimization (PSO) drives an iterative closed loop between the one-dimensional HEC-RAS model and the

Check for updates

Academic Editor: Marios Anagnostou

Received: 15 August 2026
Revised: 21 October 2026
Accepted: 26 October 2026
Published: 29 October 2026

Copyright: © 2026 by the authors. Licensee MDPI, Basel, Switzerland. This article is an open access article distributed under the terms and conditions of the Creative Commons Attribution (CC BY) license.

remote-sensing constraint to autonomously approach the optimal roughness parameters and improve the reliability of flood simulation. To bridge the scale mismatch between one-dimensional hydrodynamic outputs and two-dimensional SAR observations, the HEC-RAS cross-section geometry TIN structure is used to spatialize the simulated water surface, enabling direct comparison between simulated and SAR-observed inundation extents. The Le'an River in Wuyuan, Jiangxi Province, China, was selected as the test reach to evaluate the applicability and reliability of the framework under sparse-gauge conditions. The model was calibrated using the SAR-derived inundation extent, and simulated water levels were subsequently compared with rating-curve-derived reference levels. Under the SAR inundation constraint, the agreement between simulated and observed inundation extents improved, with IoU increasing from 0.763 under the initial parameter set to 0.789. Comparison with rating-curve-derived reference water levels further showed that the optimized Manning's roughness parameters improved water-level simulation, reducing RMSE from 0.811 m to 0.594 m and increasing NSE from 0.950 to 0.973. These results demonstrate the effectiveness of the proposed method when continuous hydrological observations are unavailable. The framework provides an automated remote-sensing-constrained approach for Manning's roughness inversion in hydrodynamic models of small and medium-sized rivers with limited in situ hydrological data.

Keywords: HEC-RAS; Manning's roughness inversion; SAR; PSO; river flood simulation

1. Introduction

Floods are among the most destructive natural hazards worldwide, posing severe threats to human life and property, infrastructure operation, and socioeconomic development. Improving the accuracy of flood forecasting and simulation is therefore an urgent requirement for flood-risk reduction. Hydrodynamic models are core tools for flood simulation and forecasting because they can explicitly reproduce flood propagation, inundation extent, and the spatial distributions of water level, depth, and velocity [1]. However, model results are affected not only by topographic accuracy, boundary conditions, and model structure, but also strongly by key parameters such as Manning's roughness [2]. Manning's roughness characterizes flow resistance in the channel bed and overbank and has significant effects on flood-wave propagation, peak evolution, water-level variation, and inundation extent [3]. Because the underlying surface conditions of natural rivers are complex, roughness is difficult to observe directly, which has long limited the accuracy of hydrodynamic flood simulation [4].

Traditional studies commonly determine Manning's roughness using Chow's empirical tables [5], comparison with photographs of typical channels [6], Cowan's composite evaluation method [7], and grain-size-based empirical formulas [8,9]. Although these methods are straightforward, they are relatively subjective, and the resulting roughness values are difficult to transfer directly to other river reaches [10]. Manual trial-and-error calibration can correct empirical values using observations, but it generally requires repeated model runs, is computationally inefficient, and remains strongly subjective [11]. To reduce the uncertainty associated with empirical assignment and manual calibration, research has increasingly shifted toward intelligent optimization algorithms for Manning's roughness calibration. In recent years, genetic algorithms (GAs), particle swarm optimization (PSO), and hybrid approaches have been applied to automated roughness calibration under complex topographic conditions [12–14]. PSO is particularly suitable for hydrody-

namic parameter optimization because of its simple formulation, small number of tuning parameters, strong global search capability, and ease of coupling with external models.

However, most existing automated calibration methods rely on continuous and complete observations of water level or discharge [15]. Gauging stations provide only point-based observations and therefore cannot adequately characterize the spatial pattern of flood inundation. Ayvaz et al. developed an automated parameter-calibration framework coupling HEC-RAS with PSO, improving the efficiency of Manning's roughness optimization; however, the optimization objective relied mainly on point hydrological observations such as water level and could not directly exploit information on the spatial expansion of flooding to constrain model parameters. Limited observations can aggravate the non-uniqueness of hydrodynamic parameter inversion and lead to parameter equifinality [16,17]. Consequently, constraining hydrodynamic models with remote-sensing observations that provide broad spatial coverage has become an important direction in flood-simulation research [18].

Synthetic aperture radar (SAR) provides all-day, all-weather, wide-area imaging and is largely unaffected by cloud and rainfall, allowing rapid acquisition of surface-water information [19–23]. Compared with conventional hydrological gauges, SAR provides spatially continuous areal information and has therefore been increasingly used for hydrodynamic model calibration and validation [24]. Hawker et al. [25] comprehensively evaluated the LISFLOOD-FP model using remote-sensing and survey data and assessed the reliability of flood simulations under different digital elevation models. Guo et al. [26] validated urban flood simulations using multi-source remote-sensing data and demonstrated that remote sensing can effectively evaluate the spatial consistency of simulated inundation extents. In these studies, however, remote-sensing data were mainly used for model evaluation or validation rather than being directly incorporated into hydrodynamic parameter optimization, leaving the spatial-constraining capability of SAR underutilized. Sadeh et al. [27] subsequently estimated surface roughness in arid environments from COSMO-SkyMed SAR backscatter and established an empirical relationship with Manning's roughness. Such estimates, however, primarily reflect land-cover and surface-roughness characteristics rather than the effective hydraulic resistance determined by the hydrodynamic response during flood propagation. More recently, SAR has gradually shifted from a post hoc validation source to a spatial constraint directly involved in parameter calibration. Wood et al. [28] calibrated the LISFLOOD-FP model using multi-temporal SAR flood extents to estimate channel depth and a spatially uniform roughness value; this approach emphasized reach-scale resistance and did not represent the spatial heterogeneity between the main channel, overbank, and different river reaches. Gobeyn et al. [29] demonstrated that the timing of SAR acquisition affects parameter constraint, but likewise used a single domain-wide roughness value, limiting representation of spatially heterogeneous resistance in natural rivers. Zotou et al. [1] developed a two-dimensional HEC-RAS calibration framework using grid search and Morris global sensitivity analysis, combining SAR inundation extent and FwDET-derived water depth for multi-metric calibration. However, the two-dimensional framework is computationally expensive, does not distinguish Manning's roughness between the main channel and overbank, and still requires a large number of model combinations, limiting efficiency in complex parameter spaces.

To address these limitations, this study proposes a new remote sensing and hydrodynamic model coupling framework centered on roughness inversion. PSO is used as the optimization engine, SAR-derived flood inundation extent is introduced as an areal spatial constraint, and an automated interface drives iterative HEC-RAS simulations. The intersection over union (IoU) between simulated and SAR-derived inundation extents is used as the objective metric to enable automated inversion of Manning's roughness. Building on the

concept of zoned roughness calibration [30], the study reach is divided into upper, middle, and lower reaches, with separate parameters for the main channel and overbank, yielding a six-dimensional Manning's roughness parameterization that represents the spatial heterogeneity of river resistance. Cross-section water-surface elevations are converted to a continuous water-surface elevation field using the HEC-RAS cross-section interpolation TIN and combined with the DEM to generate simulated inundation extents. This procedure bridges the interface between one-dimensional HEC-RAS outputs and two-dimensional SAR observations, allowing the SAR-derived inundation extent to participate directly in each parameter-search iteration and enabling automated inversion of zoned Manning's roughness in a one-dimensional HEC-RAS model.

2. Methods

2.1. Study Area

The study area is located along the main stem of the Le'an River in Wuyuan County, Shangrao City, Jiangxi Province, China. The selected reach corresponds to normalized chainages 1300–10,430 in the one-dimensional HEC-RAS (version 6.6; Hydrologic Engineering Center, U.S. Army Corps of Engineers, Davis, CA, USA) geometry and is approximately 10.7 km long. The reach passes through the urban area of Wuyuan County, including highly urbanized areas such as Binjiang Garden, Dongmen Bridge, and Ximen Bridge. The channel is sinuous, and a landscape weir is located in the middle reach. Based on these reach characteristics, the geometric model was divided longitudinally into upper, middle, and lower characteristic zones, with initial roughness values assigned separately to the main channel and overbank (Figure 1).

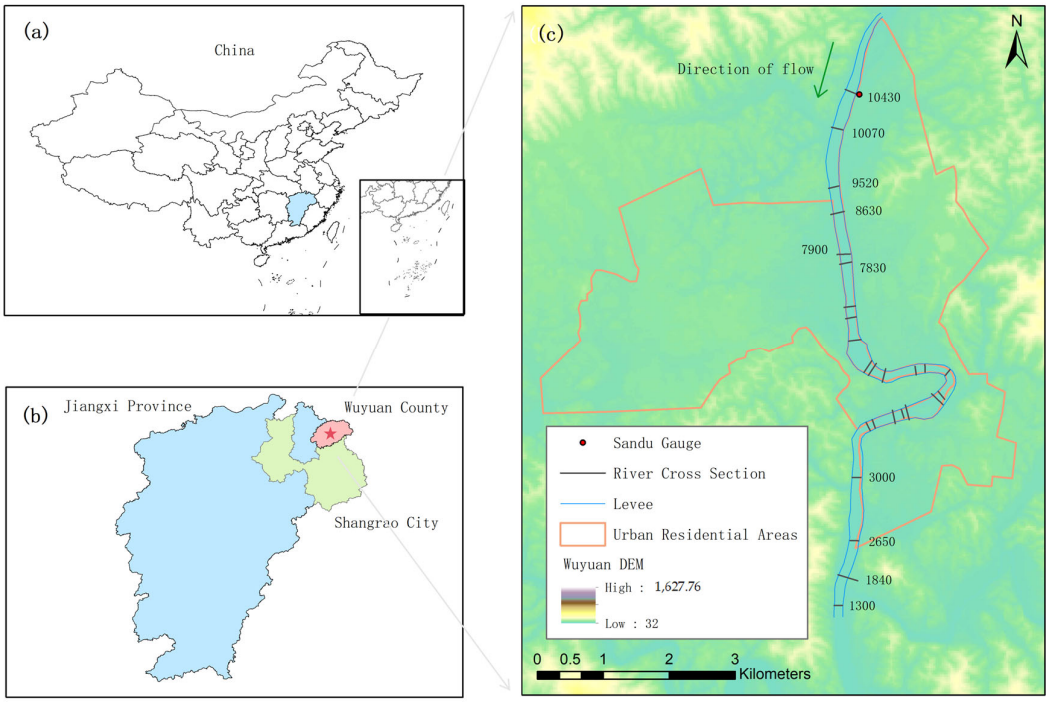

Figure 1. Overview of the study area. (**a**) Location of China and the study area (inset: South China Sea Islands); (**b**) Location of Jiangxi Province and Wuyuan County; (**c**) The studied reach of the Le'an River, showing cross-sections, the Sandu gauge, and the flow direction.

A flood event that occurred in the study area from 23 to 26 June 2017 was selected as the simulation case. Before 15:00 on 23 June, discharge remained at a relatively stable base flow of 109–140 m^3/s, with flow confined to the main channel. The river then rose rapidly from the afternoon of 23 June through 24 June, reaching a peak discharge of 5020 m^3/s

at 16:41 on 24 June and inundating riverside areas in the county town. After the peak, discharge gradually receded from the night of 24 June through 25 June and fell below 400 m^3/s on 26 June, when urban inundation had largely subsided and flow returned to the main channel. This complete rising-peak-recession sequence provides a dynamically representative case for one-dimensional unsteady-flow simulation, subsequent SAR-based calibration, and comparison with rating-curve-derived water levels.

2.2. Study Data

To construct the one-dimensional hydrodynamic model, this study integrated multiple sources of data, including field survey data, hydrological observations, remote sensing imagery, and digital elevation models. The detailed data types, sources, and their specific purposes are summarized in Table 1.

Table 1. Data used in this study.

Data Type	Data Source	Description	Purpose
Measured cross-section data	Field survey data	Station-elevation series and left/right bank coordinates for 26 measured cross-sections; acquisition time: 2 July 2017	Construction of one-dimensional hydrodynamic model geometry
Measured discharge hydrograph	Measured hydrological data from Sandu Hydrological Station	15 min measured discharge time series at the upstream station from 00:30 on 23 June 2017 to 23:45 on 26 June 2017	Upstream inflow boundary condition
Measured stage and discharge rating curve	Measured hydrological data from Sandu Hydrological Station	Stage and discharge relationship data	Model validation
Copernicus GLO-30 DEM	ESA Copernicus Data Space	Global digital surface model with 30 m spatial resolution	Construction of one-dimensional hydrodynamic model geometry
Sentinel-1 SAR imagery	ESA Copernicus Sentinel-1 platform	10 m spatial resolution; acquisition time: 18:10 Beijing Time on 25 June 2017; SAR image during the flood recession stage	Flood inundation extraction; observational data for the PSO objective function

Data Preprocessing

To ensure consistency among multisource datasets, all spatial data were projected to the CGCS2000 3-degree Gauss–Kruger CM117E coordinate system, with meters used consistently for horizontal and vertical units. The Copernicus GLO-30 DEM product is a digital surface model (DSM) that includes building and vegetation elevations. Measured cross-sections were used to correct channel elevations, but no building-specific elevation correction was applied. Sentinel-1 SAR imagery was subjected to radiometric calibration, filtering, geometric correction, and projection transformation before flood inundation extraction. Hydrological time series were resampled to a 15 min interval, and Beijing Time was adopted as the common time reference to ensure spatio-temporal consistency among hydrological observations, remote-sensing observations, and hydrodynamic simulations.

2.3. Hydrodynamic Modeling and Manning's Roughness Inversion

2.3.1. Remote Sensing Hydrodynamic Model Coupling Framework

This study proposes a new remote sensing and hydrodynamic model coupling framework centered on roughness inversion (Figure 2). First, flood inundation extent is extracted from Sentinel-1 SAR imagery and used as the spatial observational constraint. Manning's roughness values for different river reaches are then treated as parameters to be optimized, and the one-dimensional HEC-RAS model is driven for forward hydrodynamic simulation. An objective function is constructed from the intersection over union between the simulated

inundation extent and the SAR-observed extent, and the resulting evaluation is fed back to PSO to continuously update candidate roughness parameters until the convergence criterion is satisfied or the maximum number of iterations is reached. The resulting optimal parameters are finally reintroduced into the hydrodynamic model for continuous flood-process simulation and compared with water levels derived from the measured stage and discharge relationship. This workflow forms a technical closed loop of "remote-sensing observation–constraint construction–roughness inversion–model simulation–simulation validation". The framework is designed to reduce the dependence of Manning's roughness calibration on dense, continuous gauge observations while improving the spatial representativeness and hydraulic plausibility of the inverted parameters.

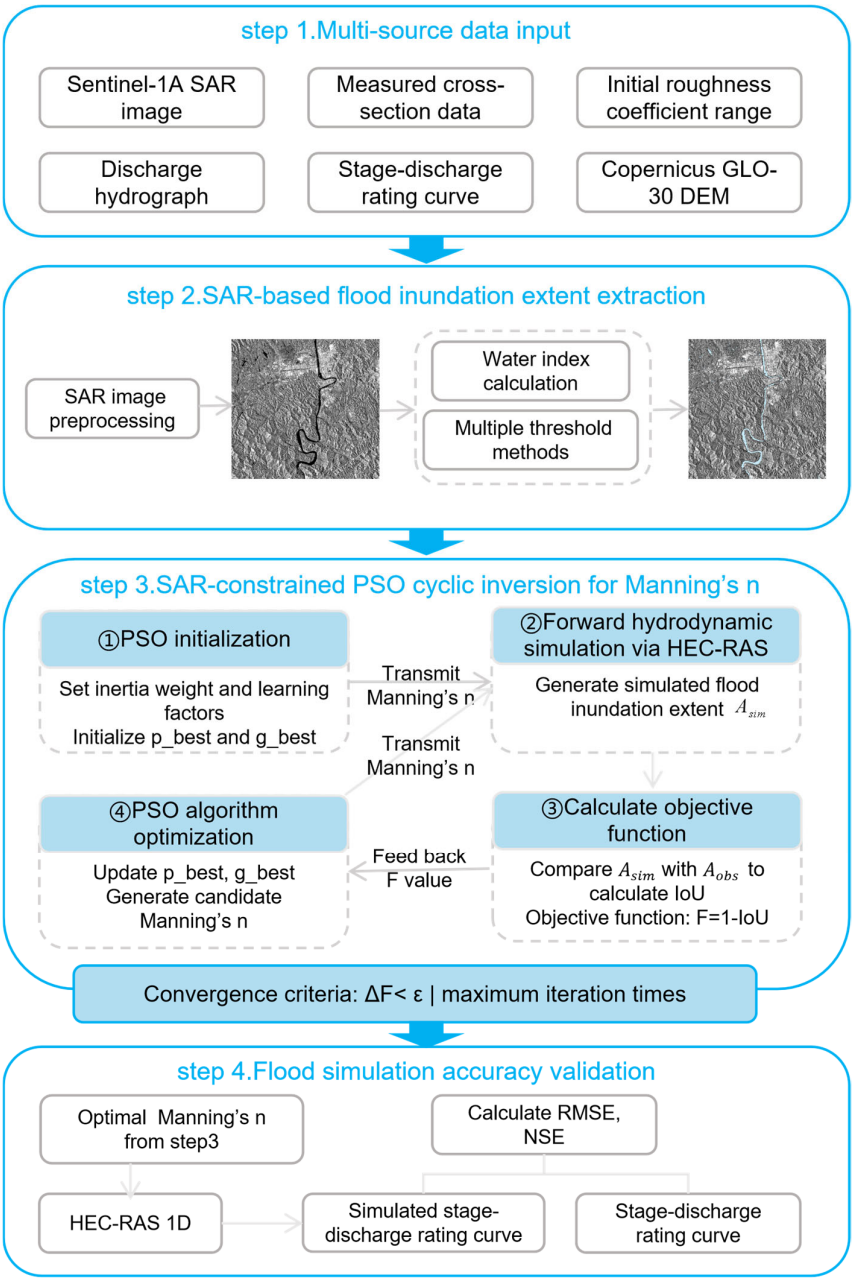

Figure 2. Remote sensing and hydrodynamic model coupling framework.

2.3.2. One-Dimensional Hydrodynamic Model Setup

HEC-RAS 6.6 was used to establish a one-dimensional unsteady-flow hydrodynamic model of the study reach to simulate flood propagation along the river and the associated variations in water level, discharge, and inundation extent. The model setup includes

governing equations, geometric representation, boundary and initial conditions, Manning's roughness parameterization, and model-output settings [31,32].

One-dimensional unsteady flow is described by the Saint-Venant equations, comprising the continuity equation based on mass conservation and the momentum equation based on momentum conservation:

$$\frac{\partial A}{\partial t} + \frac{\partial Q}{\partial x} = q_l \tag{1}$$

$$\frac{\partial Q}{\partial \mathrm{t}} + \frac{\partial}{\partial x}\left(\frac{\beta Q^2}{A}\right) + gA\frac{\partial H}{\partial x} + gAS_f = 0 \tag{2}$$

where A is the cross-sectional flow area (m^2); Q is discharge (m^3/s); x and t denote the spatial coordinate and time, respectively; q_l is lateral inflow per unit channel length (m^2/s); β is the momentum correction coefficient; H is water-surface elevation (m); g is gravitational acceleration (m/s^2); and S_f is the friction slope.

The friction slope is calculated using Manning's equation:

$$S_f = \frac{n^2 Q|Q|}{A^2 R^{4/3}} \tag{3}$$

where n is Manning's roughness coefficient and R is the hydraulic radius. Thus, Manning's roughness directly affects channel velocity, water level, and flood propagation through the friction term and is therefore the primary model parameter inverted in this study.

HEC-RAS numerically solves the one-dimensional unsteady-flow equations using an implicit finite-difference method, obtaining water level and discharge at each time step through linearization and iterative computation. This solution scheme provides good numerical stability.

The one-dimensional geometric model of the study reach consists of the river centerline, left and right bank lines, flow paths, and cross-sections. Cross-section data describe the geometry of the main channel and the left and right overbanks. A total of 26 measured cross-sections were used. The surveyed elevations and the Copernicus GLO-30 DEM were transformed to the same horizontal coordinate system. The measured cross-sections were primarily used to represent channel geometry, while the DEM supplemented the terrain on both banks and supported subsequent inundation mapping from the one-dimensional water surface.

The measured discharge hydrograph from 23 to 26 June 2017 was specified as the upstream boundary to represent flood inflow. A normal-depth condition was applied at the downstream boundary, with an energy slope of 0.004428 m/m, estimated from the mean longitudinal bed slope between cross-sections RS1840 and RS1300. HEC-RAS used this slope together with Manning's equation to calculate the downstream boundary depth.

The simulation period was set from 00:30 on 23 June 2017 to 23:30 on 26 June 2017, with a computational time step of 1 min. To reduce water-level and discharge oscillations caused by inconsistencies in the initial conditions, 100 warm-up time steps were applied before the formal simulation. Each warm-up step was 0.008333 h, corresponding to a total warm-up duration of approximately 50 min. The warm-up procedure does not advance the formal simulation time; instead, it establishes a relatively stable initial distribution of water level and discharge under the starting boundary conditions. The water-level convergence tolerance was set to 0.006 m, with a maximum of 20 iterations per time step.

Considering longitudinal differences in channel-bed composition, cross-sectional morphology, and overbank characteristics, the study reach was divided into nine roughness zones, each associated with a Manning's roughness parameter. Within each cross-section, the resistance characteristics of the left overbank, main channel, and right overbank were distinguished. Because the left and right overbank roughness values were set equal, the

parameters actually optimized were the main-channel and overbank Manning's roughness values for the upper, middle, and lower reaches, yielding a total of six roughness parameters. The cross-sectional roughness zoning and the spatial distribution of the upper, middle, and lower reaches are shown in Figure 3. The landscape weir and bridges were not explicitly represented as hydraulic structures. The estimated Manning's *n* values may therefore partly compensate for their unresolved hydraulic effects and should be interpreted as effective reach-scale roughness parameters.

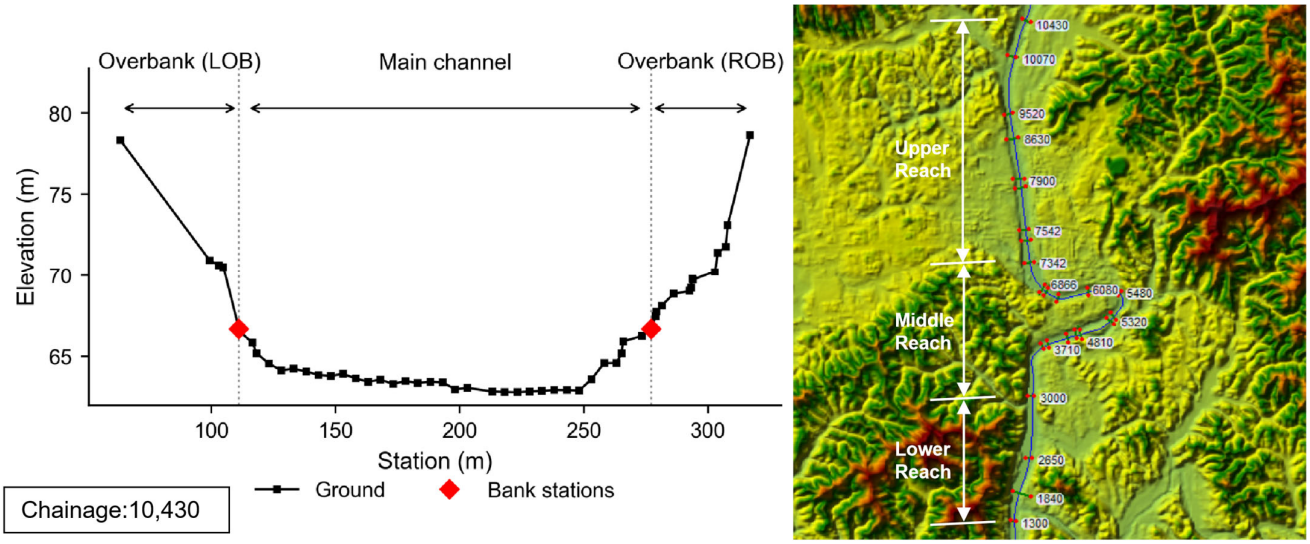

Figure 3. Manning's roughness zoning across the river cross-section and spatial distribution of the upper, middle, and lower reaches.

Initial values for the roughness parameters to be inverted were determined from the literature, the Cowan method, and the underlying surface characteristics of the study reach, as summarized in Table 2.

Table 2. Initial Manning's roughness values for the natural river.

River Reach	Characteristics	Main Channel	Overbank
Upper reach 7342–10,430	Relatively straight channel; dense trees, shrubs, and other vegetation on both overbanks	0.052	0.085
Middle reach 3000–7342	Large river bend; mixed woodland and built-up land on both overbanks	0.064	0.084
Lower reach 1300–3000	Relatively straight channel; overbanks dominated by low herbaceous vegetation with few tall shrubs	0.085	0.072

During PSO inversion, river geometry, boundary conditions, computational time step, and all other model settings were held constant; only the Manning's roughness values of the individual zones were updated. For each candidate parameter set, the model output the water-surface elevation at the SAR overpass time, which was combined with the terrain to generate a simulated inundation extent. Candidate parameters were evaluated using the IoU between simulated and SAR-observed inundation extents, and the optimal Manning's roughness combination was ultimately identified.

The internal computational time step was 1 min, the output interval for water level and discharge time series was 15 min, and the detailed hydraulic-results output interval was 1 h. To accurately extract the simulated inundation extent at the Sentinel-1 SAR overpass time of 18:10 on 25 June 2017, the mapping-output interval was set to 10 min.

The model produced water level, discharge, and other hydraulic variables at each calculation time and generated spatial distributions of water-surface elevation, water depth, and velocity in RAS Mapper [33]. The Depth layer at the SAR overpass time was used to extract the simulated flood inundation extent and calculate IoU, while water-surface elevation outputs were used to construct the simulated stage and discharge relationship for comparison with rating-curve-derived water levels.

2.3.3. SAR-Derived Flood Inundation Extent

Synthetic aperture radar (SAR), as an active microwave imaging system, provides all-day and all-weather observations, has penetration capability, and is insensitive to cloud cover, allowing stable surface observations when optical imagery is affected by weather or illumination. SAR is therefore an important data source for dynamic flood-water monitoring, with Sentinel-1 being among the most widely used missions.

Sentinel-1 GRD imagery was used to extract the flood inundation extent [34]. The SAR image was first subjected to orbit correction, radiometric calibration, speckle filtering, and terrain correction to reduce systematic errors and improve image quality. The preprocessed image was then clipped to the study area and projected to CGCS2000 3-degree Gauss–Kruger CM117E to ensure spatial consistency among the SAR image, terrain data, and HEC-RAS simulation results.

Gray-level threshold segmentation of SAR imagery exploits the low backscatter and dark appearance of relatively smooth water surfaces to classify pixels into water and non-water categories [35–37]. To reduce dependence on a single water feature, four SAR-derived features were compared: VV-polarized backscatter, the polarization ratio (VH/VV) [38], the normalized difference polarization index (NDPI) [39–41], and the Sentinel-1 dual-polarized water index (SDWI) [42]. Visual comparison indicated that VH/VV and NDPI provided limited water–land contrast in this image; therefore, they were used for feature comparison but were not retained for constructing the final inundation extent.

$$NDPI = \frac{VV - VH}{VV + VH} \tag{4}$$

$$SDWI = \ln(10 \cdot VV \cdot VH) - 8 \tag{5}$$

In Equation (5), ln denotes the natural logarithm, and VV and VH are dimensionless linear backscatter coefficients. The input backscatter values in decibels were converted to the linear scale using $VV = 10^{VV_{dB}/10}$ and $VH = 10^{VH_{dB}/10}$ before calculating SDWI.

This study first conducted a statistical analysis using typical water bodies and surrounding non-water areas within the study region to determine the pixel response ranges for various SAR water-feature components; it then established segmentation thresholds by incorporating the actual inundation characteristics of the flood event. The adopted water-classification conditions were $VV_{dB} \leq -14$ dB and SDWI ≤ -13, with SDWI being dimensionless.

The final remote-sensing-observed inundation extent was determined by integrating the extraction results from the different SAR water features and thresholding methods. Here, integration refers to visual comparison and selection rather than pixelwise combination of the binary masks. The SDWI extraction result was selected as the base mask for subsequent manual refinement in ArcGIS (version 10.7; Environmental Systems Research Institute, Redlands, CA, USA). The $VV_{dB} \leq -14$ dB result was used only for visual comparison during feature selection and was not incorporated into the final inundation map. Water bodies not belonging to the river were removed. Because the terrain data used in the hydrodynamic model cannot accurately represent exposed in-channel features such as reefs, these features were incorporated into the inundated area. River water outside cross-

sections 10430 and 1300 was clipped to ensure comparability in spatial detail between observations and simulations. The resulting inundation extent (Figure 4) was used as the spatial constraint for subsequent objective-function construction and Manning's roughness inversion. The final extent was not independently assessed against contemporaneous reference data because such data were unavailable; manual refinement should not be interpreted as an independent accuracy assessment.

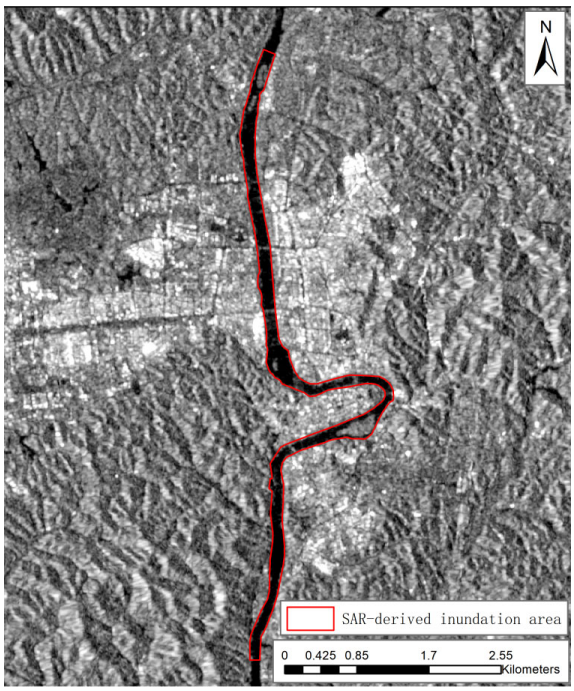

Figure 4. Final remote-sensing-observed flood inundation extent.

2.3.4. Spatial Transformation of One-Dimensional Simulation Results and Objective-Function Construction

To effectively constrain the hydrodynamic model with remote-sensing observations, an objective function is required that reflects the spatial agreement between simulated and observed results. Traditional roughness calibration relies mainly on point observations such as water level and discharge, which have limited spatial representativeness and cannot effectively constrain flood inundation. In contrast, SAR imagery provides a spatially continuous distribution of flood inundation. Therefore, the SAR-derived observed inundation extent was used as the spatial constraint for model calibration.

To allow the SAR flood extent to participate directly in parameter optimization of the one-dimensional hydrodynamic model, the discrete cross-sectional water-surface elevations output by HEC-RAS must first be converted into a simulated inundation extent that can be compared spatially with SAR observations. Water-surface elevations at each cross-section at the SAR acquisition time were extracted from HEC-RAS results. Based on the spatial topology of cross-sections in the HEC-RAS geometry file and the cross-section interpolation TIN structure, water-surface elevations between adjacent cross-sections were spatially interpolated to construct a continuous water-surface elevation field. This field was then differenced with the DEM:

$$D(x,y) = WSE(x,y) - DEM(x,y) \quad (6)$$

where D(x,y) is the simulated water depth at location (x,y). When D(x,y) > 0.1 m, the corresponding grid cell is classified as inundated, thereby generating the simulated inundation extent A_{sim} for the current Manning's roughness combination. No building-specific

elevation correction was applied. At the SAR acquisition time, the inundation extent did not reach the building areas; therefore, building elevations were not expected to materially affect the inundation mask used for IoU calculation. This spatial transformation is used only to construct the SAR spatial constraint and calculate the objective function during PSO iterations.

The intersection over union (IoU) was used to evaluate the spatial overlap between simulated and observed inundation extents. IoU ranges from 0 to 1, with larger values indicating greater agreement between simulation and observation, and is calculated as

$$IoU = \frac{|A_{sim} \cap A_{obs}|}{|A_{sim} \cup A_{obs}|} \tag{7}$$

where A_{sim} denotes the simulated inundation extent and A_{obs} denotes the remote sensing observed inundation extent.

Because PSO minimizes the objective function, the objective function in this study was defined as

$$F = 1 - IoU \tag{8}$$

The optimization minimizes the objective function and outputs the optimal set of spatially distributed Manning's roughness parameters.

2.3.5. IoU-Based Automated PSO Inversion of Manning's Roughness

To automate Manning's roughness calibration, particle swarm optimization (PSO) was employed with F = 1 − IoU as the objective function, establishing a closed-loop optimization framework between the SAR-derived flood inundation extent and the one-dimensional HEC-RAS hydrodynamic model. Each particle represents a candidate set of Manning's roughness parameters. The nine spatial roughness zones of the river correspond to six roughness parameters; particle velocity represents the direction and magnitude of parameter updates, while particle position represents the current roughness combination.

The PSO parameters were set as follows: swarm size = 20, maximum number of iterations = 20, inertia weight = 0.9, acceleration coefficients $c_1 = c_2 = 1.4962$ and $\varepsilon = 1 \times 10^{-6}$. The velocity limit was dynamically set to 30% of the width of each parameter search interval. The initial swarm was generated by random uniform perturbations around the initial roughness values, with a perturbation amplitude equal to 15% of each parameter search interval. Boundary clipping was then applied to ensure that all initial solutions remained within the search space and were well distributed. These settings were informed by the PSO calibration study of Shahverdi and Talebmorad [30], whose recommended inertia weight and acceleration coefficients were adopted from their sensitivity analysis. Swarm size and iteration number were selected to balance computational cost and convergence while sufficiently exploring the parameter space under a limited computational budget.

The search ranges in Table 3 were specified with reference to the initial roughness estimates and reach characteristics, restricting optimization to a prescribed parameter domain under a limited computational budget. The main-channel lower bounds of 0.050–0.060 reflect the relatively high initial roughness estimates adopted for this reach. The resulting parameter estimates are conditional on these bounds, and lower values outside the prescribed ranges were not evaluated.

During each iteration, the roughness parameters represented by a particle were first written to the HEC-RAS geometry file. HEC-RAS was then automatically called through the command line to perform the unsteady-flow simulation, and RAS Mapper generated the flood inundation extent by interpolating the simulated water levels. IoU was calculated between the simulated and SAR-observed inundation extents and converted to the objective-function value. Particle velocities and positions were then updated according to

each particle's personal best position and the swarm's global best position, progressively searching for the globally optimal roughness combination. The algorithm terminated when the maximum number of iterations was reached or the change in the objective function became negligible, and the optimal Manning's roughness parameters were output.

Table 3. PSO search ranges for Manning's roughness in the natural river.

River Reach	Characteristics	Main Channel	Overbank
Upper reach 7342–10,430	Relatively straight channel; dense trees, shrubs, and other vegetation on both overbanks	[0.050, 0.072]	[0.070, 0.092]
Middle reach 3000–7342	Large river bend; mixed woodland and built-up land on both overbanks	[0.060, 0.080]	[0.068, 0.088]
Lower reach 1300–3000	Relatively straight channel; overbanks dominated by low herbaceous vegetation with few tall shrubs	[0.060, 0.085]	[0.067, 0.087]

An automated roughness-inversion workflow of "SAR observation–HEC-RAS simulation–IoU evaluation–PSO update" was developed. First, the observed flood inundation extent was extracted from SAR imagery. Second, HEC-RAS was automatically updated with the Manning's roughness values represented by each particle and the flood simulation was executed. Third, IoU between the simulated and SAR-observed inundation extents was calculated as the particle fitness. Finally, PSO updated particle positions and proceeded to the next iteration until the convergence criterion was met, yielding the optimal roughness combination. The inversion loop is automated, while preparation of the SAR observation constraint includes manual editing in ArcGIS (Figure 5).

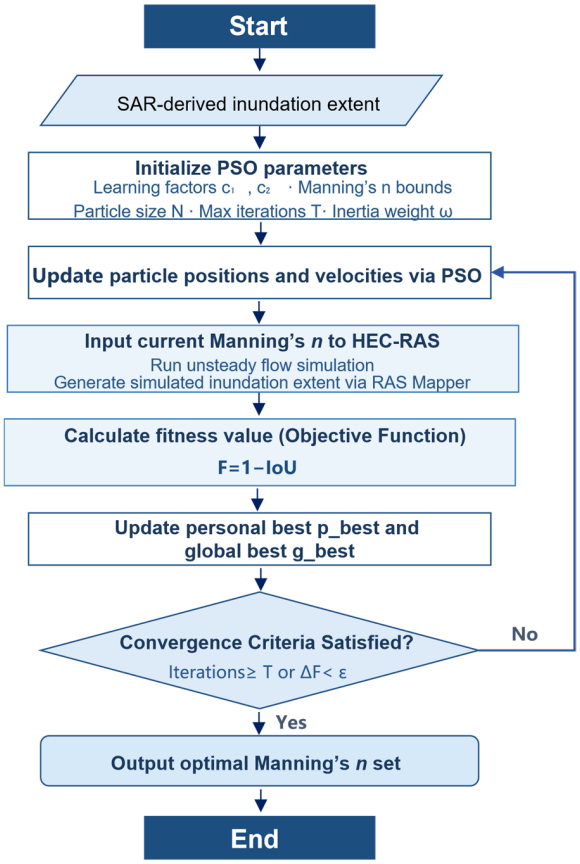

Figure 5. Flowchart of the PSO-based Manning's roughness inversion algorithm constrained by SAR-derived inundation extent.

3. Results

3.1. Convergence Characteristics of PSO-Based Manning's Roughness Inversion

To evaluate the optimization performance of the proposed remote sensing and hydrodynamic model coupling framework centered on roughness inversion, the convergence behavior of PSO was analyzed using the objective function F = 1 − IoU. As shown in Figure 6, the initial objective-function value was 0.237, corresponding to an IoU of 0.763 between the simulated and SAR-observed inundation extents. After iterative optimization, the objective function decreased to 0.211 and the corresponding IoU increased to 0.789. The objective function decreased by 10.9%, indicating that PSO effectively searched the Manning's roughness parameter space and identified a more suitable parameter combination. No independent PSO runs with different random seeds were performed; therefore, the statistical significance of the reported improvement relative to run-to-run variability remains unassessed.

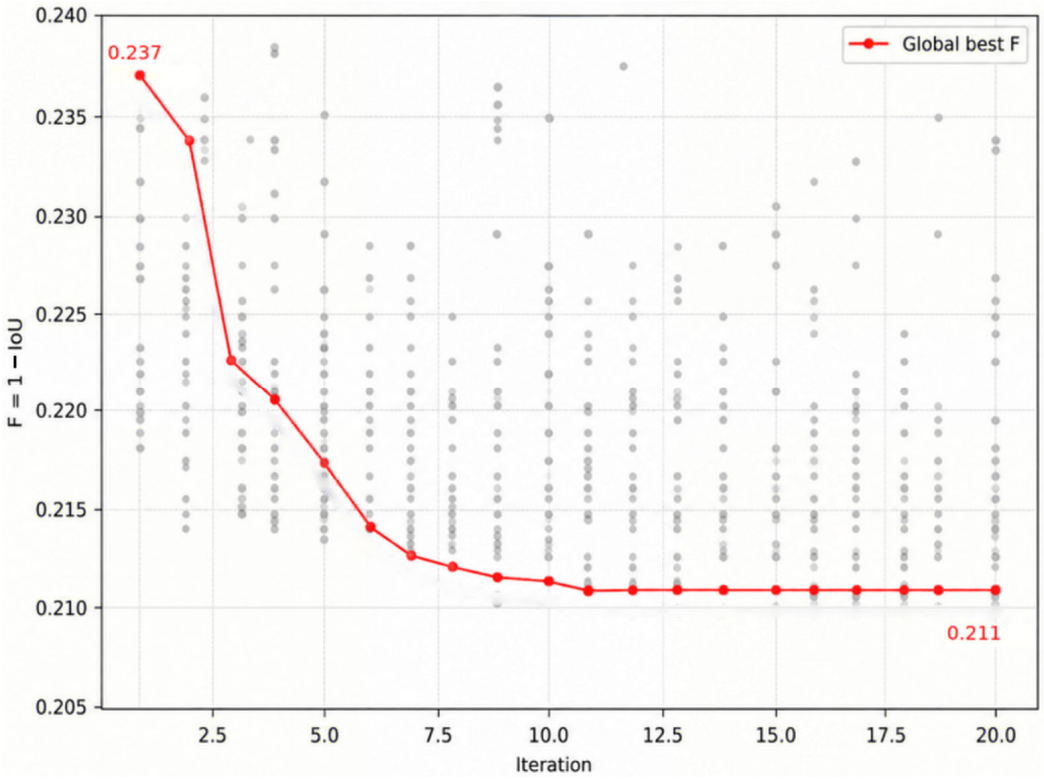

Figure 6. Variation in the global best objective function during PSO iterations.

During the early optimization stage, the objective function decreased rapidly, indicating that PSO effectively adjusted Manning's roughness from the initial estimates. After the 10th iteration, changes in the global best solution became small, indicating that the optimization had reached a stable state. This convergence behavior demonstrates that the proposed framework can automatically identify Manning's roughness combinations constrained by the SAR-observed inundation extent.

To further examine the associations between Manning's roughness and the objective function, an exploratory regression analysis was conducted using the six optimized roughness parameters and their corresponding objective-function values from the PSO search samples (Figure 7).

To further analyze the response of zoned Manning's roughness parameters to the SAR-based spatial objective function, multiple linear regression was performed using the parameter combinations and corresponding objective-function values generated during PSO iterations. Because the objective function is defined as F = 1 − IoU, a negative t-statistic

indicates that, after accounting for the joint effects of the other parameters, an increase in that parameter is generally associated with a decrease in F, i.e., improved spatial agreement between simulated and SAR-observed inundation extents; a positive t-statistic indicates the opposite response direction. The magnitude of the t-statistic reflects the estimated regression coefficient relative to its standard error, rather than directly measuring physical sensitivity. Because the samples were generated through adaptive PSO searches, the regression statistics are interpreted as exploratory results within the sampled parameter space.

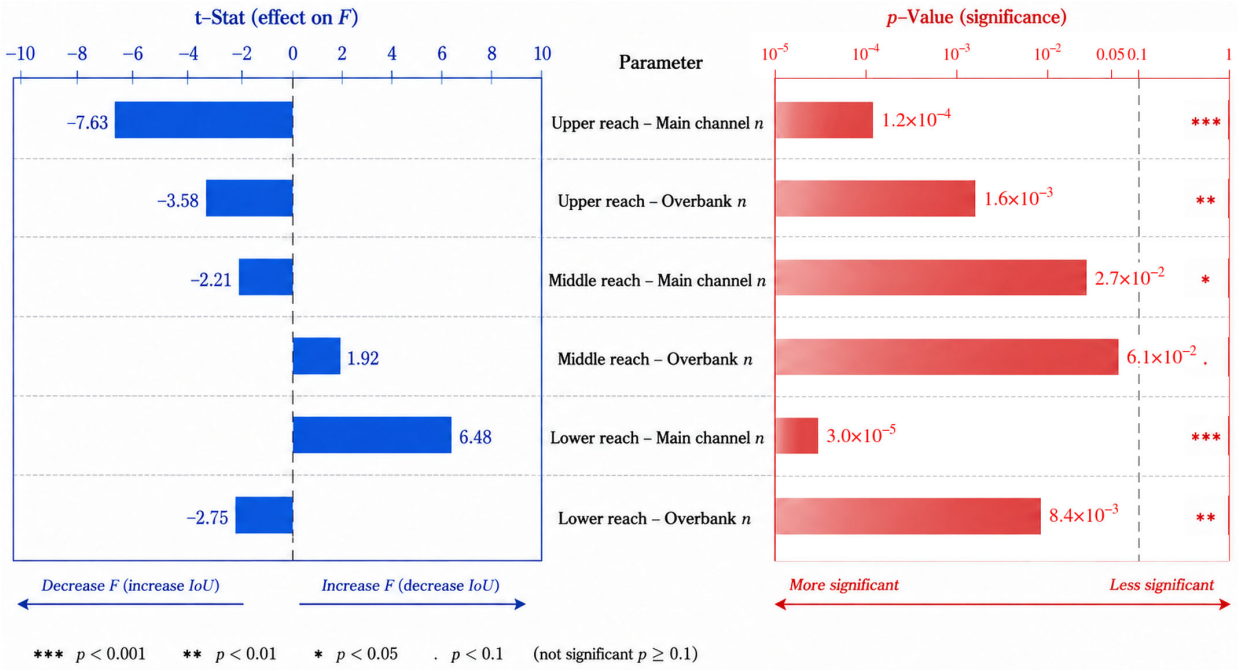

Figure 7. Regression t-statistics and nominal *p*-values for the six Manning's roughness parameters based on PSO search samples.

The six roughness parameters exhibited clearly different responses to the objective function. Upper-reach main-channel roughness showed the largest absolute negative t-statistic, with higher values associated with improved spatial agreement within the sampled parameter combinations. In contrast, lower-reach main-channel roughness showed a positive association with F, with higher values associated with reduced agreement. Upper- and lower-reach overbank roughness also showed negative associations with nominal *p*-values below 0.05, but their |t-statistics| were markedly smaller than those of the main-channel parameters. Middle-reach main-channel roughness had a nominal *p*-value below 0.05, although its |t-statistic| was clearly smaller than those of the upper- and lower-reach main-channel parameters. Middle-reach overbank roughness had the smallest |t-statistic|, with a nominal *p*-value above 0.05. This result is specific to the sampled parameter combinations and the fitted linear model and does not establish the identifiability of the overbank parameter.

These results demonstrate that the SAR-derived inundation extent constrains Manning's roughness differently among reaches and between the main channel and overbank. Main-channel Manning's roughness in the upper and lower reaches exhibited pronounced conditional linear associations with the objective function within the parameter combinations explored by PSO. Overbank roughness generally has a weaker response than main-channel roughness, while the independent contribution of roughness in the middle reach is relatively limited, reflecting the spatially variable influence of resistance changes on flood-inundation patterns. The six Manning's roughness parameters therefore exhibit differentiated regression responses within the sampled parameter space. This analysis pro-

vides an exploratory interpretation of the zoned Manning's roughness parameter responses during optimization.

3.2. Improvement in Inundation Simulation After Manning's Roughness Optimization

To further evaluate the effectiveness of the proposed SAR-constrained Manning's roughness inversion method, the spatial distributions of simulated flood depth before and after optimization were compared with the SAR-observed inundation extent (Figure 8). The initial simulation using empirically assigned Manning's roughness produced an IoU of 0.763 with the SAR-observed extent. After PSO inversion constrained by SAR, the simulated IoU increased to 0.789, an absolute improvement of 0.026 (2.58 percentage points).

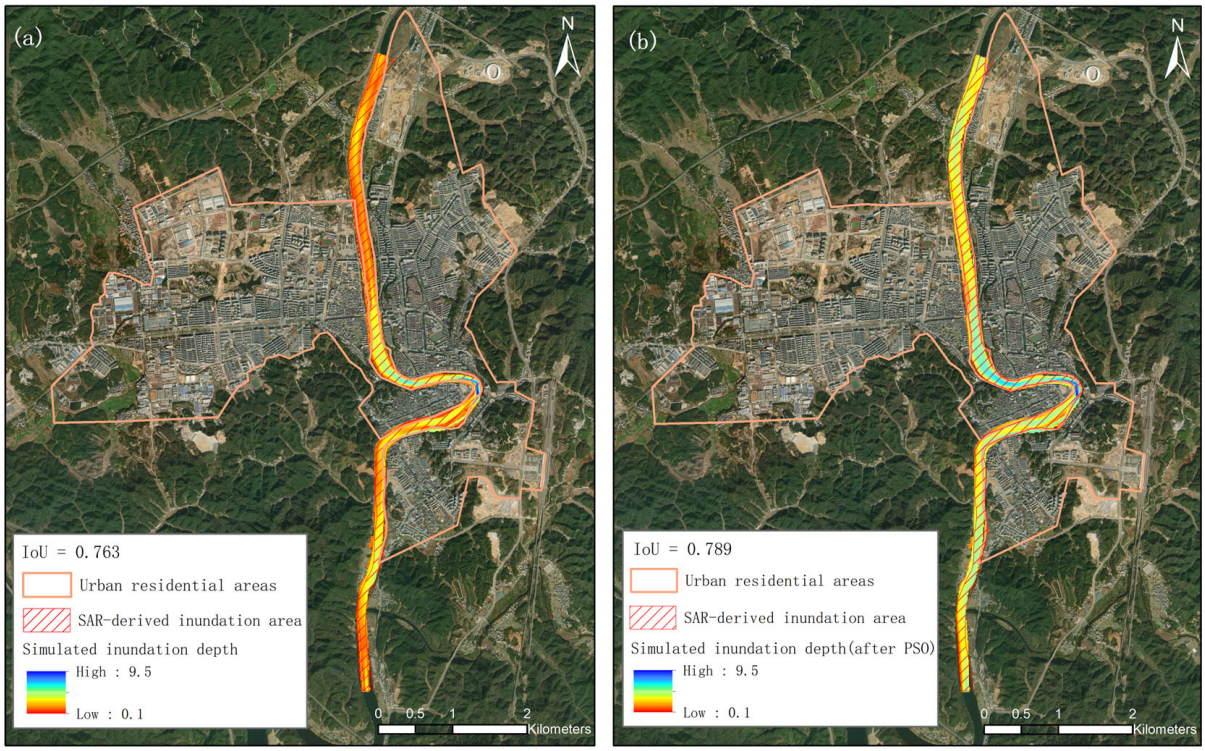

Figure 8. Comparison of simulated results before and after PSO of Manning's roughness under the SAR inundation constraint: (**a**) simulation using the initial Manning's roughness values; (**b**) simulation using the PSO-optimized Manning's roughness values. Colors represent simulated inundation depth (m), and red hatching denotes the SAR-derived inundation extent.

Before optimization, the simulated inundation extent differed from the SAR-derived extent, particularly in the upper reach and near river bends (Figure 8a). The initial empirical roughness values caused underestimation of flood depth in several areas, resulting in disagreement between simulation and remote-sensing observations. After PSO parameter optimization, the simulated inundation extent agreed more closely with the SAR-observed extent, and mismatch areas along the flood boundary were reduced (Figure 8b). Using $F = 1 - \text{IoU}$ as the objective function, PSO was applied to invert the main-channel and overbank Manning's roughness values for each reach. The resulting optimal parameters are listed in Table 4.

The improvement in inundation-extent agreement was relatively limited because the SAR image used in this study was acquired at 18:10 Beijing Time on 25 June 2017, during the flood recession stage. By that time, floodwater had largely returned to the main channel, inundation extent was controlled mainly by channel geometry, and overbank flow accounted for only a small portion of the flow. Consequently, changes in Manning's

roughness primarily affected hydraulic variables such as water depth and velocity and produced only limited changes in the total inundated area.

Table 4. Optimal Manning's roughness values obtained by PSO.

River Reach	Characteristics	Main Channel	Overbank
Upper reach 7342–10,430	Relatively straight channel; dense trees, shrubs, and other vegetation on both overbanks	0.062	0.080
Middle reach 3000–7342	Large river bend; mixed woodland and built-up land on both overbanks	0.072	0.078
Lower reach 1300–3000	Relatively straight channel; overbanks dominated by low herbaceous vegetation with few tall shrubs	0.073	0.077

Nevertheless, the optimized Manning's roughness values altered the hydraulic response of the model by adjusting flow resistance in different reaches. Compared with the initial parameterization, the optimized simulation produced a more physically plausible spatial distribution of flood depth. To further evaluate model performance, simulated water levels at cross-section RS10430 were compared with reference levels derived from the station's stage–discharge relationship.

3.3. Comparison with Rating-Curve-Derived Water Levels

Although the improvement in inundation extent was limited because the SAR observation corresponded to the flood recession stage, Manning's roughness inversion primarily modifies the hydraulic response of the model, including the stage and discharge relationship. Water levels at cross-section RS10430 were compared over 23–26 June 2017 with reference water levels derived from the station's stage and discharge relationship. The discharge record used to derive these reference levels was also used to specify the upstream inflow boundary.

Simulated water levels before and after Manning's roughness optimization were extracted from HEC-RAS and compared with water levels derived from the measured stage and discharge rating curve (Figure 9). Root mean square error (RMSE) and the Nash Sutcliffe efficiency (NSE) were used to evaluate the initial and optimized simulations. The comparison shows that the optimized Manning's roughness parameters improved agreement between the simulated and rating-curve-derived water levels, with RMSE decreasing from 0.811 m to 0.594 m and NSE increasing from 0.950 to 0.973. The peak reference water level was about 78.8 m, whereas the simulated peak water levels were about 76.8 m before optimization and 77.4 m after optimization, so the peak remained underestimated by about 1.4 m after optimization.

Unlike the inundation-extent comparison, comparison with rating-curve-derived water levels directly reflects the sensitivity of hydraulic simulation results to Manning's roughness. The optimized roughness values effectively reduced systematic bias in simulated water levels, with clear improvements during the rising stage. Near the peak, however, the simulated water level remained lower than the rating-curve-derived reference level, indicating that the peak water level is still underestimated after optimization.

These results confirm that SAR-observed inundation provides an effective spatial constraint for Manning's roughness inversion, while measured water-level data provide comparison with rating-curve-derived water levels of hydraulic performance. Combining remote-sensing observations with in situ hydraulic data can reduce dependence on dense, continuous gauge observations for Manning's roughness calibration while improving the spatial representativeness and hydraulic plausibility of the inverted parameters.

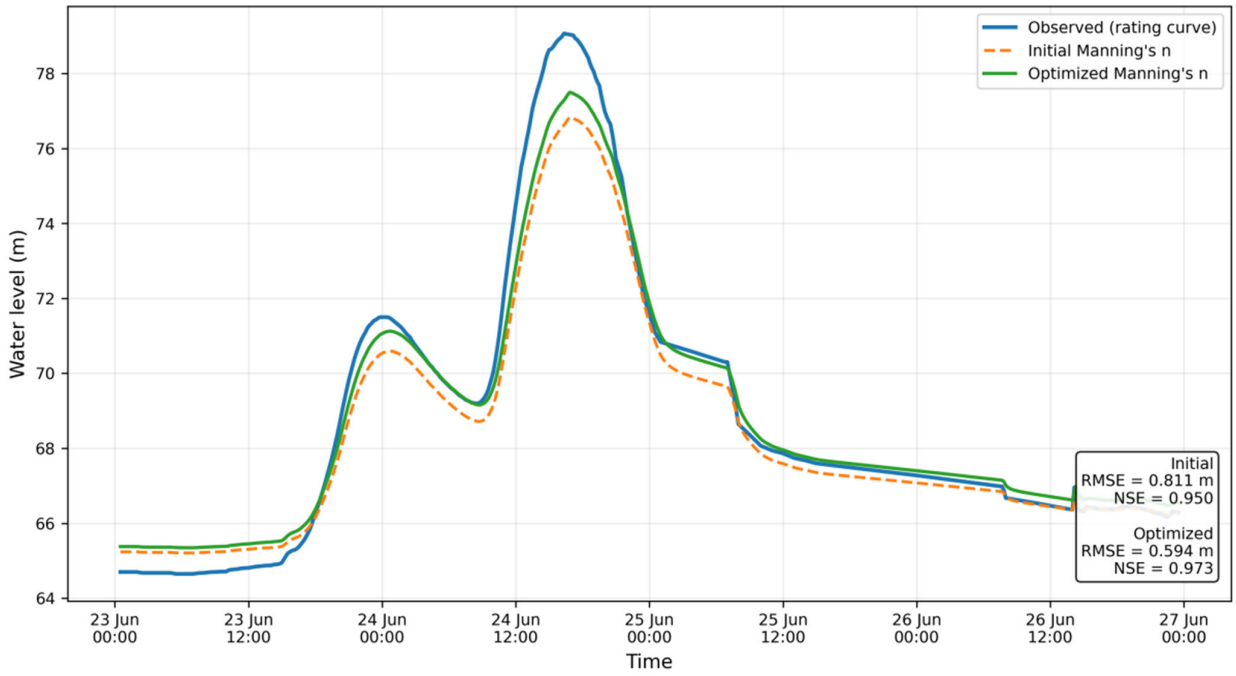

Figure 9. Comparison of simulated water levels before and after Manning's roughness optimization with rating-curve-derived reference water levels at cross-section RS10430.

4. Discussion

4.1. Effectiveness of SAR-Derived Inundation Extent for Constraining Manning's Roughness Inversion

The accuracy of flood hydrodynamic simulation depends strongly on the representation of river resistance. Manning's roughness is commonly assigned from empirical land-cover information or values reported in previous studies. Such approaches are unable to adequately represent the spatiotemporal heterogeneity of Manning's roughness and can introduce substantial parameter uncertainty, particularly in natural rivers with pronounced spatial differences between channel and overbank conditions.

In this study, SAR-derived inundation extent was introduced directly into Manning's roughness inversion as a spatial constraint. Unlike conventional calibration approaches that rely only on hydrological observations from a limited number of gauges, SAR provides spatial information on flood distribution, allowing hydraulic parameters to be constrained by observed flood patterns.

The results show that the SAR-constrained PSO framework effectively adjusted Manning's roughness and improved agreement between simulated flood characteristics and remote-sensing observations. Although the SAR image used in this study was acquired during the flood recession stage, the optimization still reduced discrepancies between the simulated and SAR-derived inundation boundaries. This demonstrates that remote-sensing observations can provide valuable spatial information for reducing uncertainty in hydraulic-model parameters and have important application potential in data-scarce basins lacking continuous hydrological observations.

In addition, this study developed an automated coupling strategy between remote-sensing observations and hydraulic simulation. By incorporating SAR-derived inundation extent into the objective function, the optimization directly links observable flood spatial patterns with hydraulic parameters, providing an alternative to conventional manual Manning's roughness calibration with stronger spatially based physical constraints.

4.2. Reasons for the Limited Improvement in Spatial IoU

After Manning's roughness optimization, the IoU between the simulated and SAR-derived inundation extents increased from 0.763 to 0.789. Although this improvement is modest compared with that reported in some flood-mapping studies, it does not indicate poor performance of the proposed method. The hydraulic conditions at the SAR acquisition time offer a possible explanation for the limited improvement, but their contribution has not been isolated from other sources of uncertainty, including PSO run-to-run variability.

The Sentinel-1 SAR image used in this study was acquired during the flood recession stage, when floodwater had largely retreated from the overbank and inundation extent was controlled mainly by channel geometry. Under these conditions, changes in Manning's roughness primarily affect hydraulic variables such as water level, velocity, and depth, while their influence on the spatial inundation extent is relatively small.

The comparison with rating-curve-derived water levels further supports this interpretation. Although the improvement in IoU was limited, water-level simulation became more reasonable with the optimized roughness parameters. This indicates that evaluating hydraulic-parameter optimization solely from inundation extent may underestimate the actual effect of Manning's roughness inversion; spatial and hydraulic observations should therefore be combined in a multi-metric evaluation framework.

5. Conclusions

This study coupled a one-dimensional HEC-RAS hydraulic model with a SAR-constrained PSO framework for Manning's roughness inversion and flood simulation. The main conclusions are as follows:

(1) The SAR-derived inundation extent was embedded in HEC-RAS simulation to establish a remote sensing and hydrodynamic coupling framework. Manning's roughness parameters were automatically updated through PSO, enabling efficient, automated parameter calibration compared with conventional empirical assignment.

(2) SAR-constrained PSO inversion yielded spatially distributed optimal Manning's roughness values. Agreement between the optimized simulated flood pattern and SAR observations improved, with IoU increasing from 0.763 to 0.789. This demonstrates that SAR observations can provide reliable spatial constraints for hydraulic-parameter estimation.

(3) Comparison with water levels derived from the measured stage and discharge relationship showed that the optimized Manning's roughness improved the hydraulic response of the model. Although the recession-stage SAR image limited the improvement in inundation extent, the optimized model produced more reasonable water-level simulations and better represented channel resistance.

(4) By integrating remote-sensing observations with hydrodynamic simulation, the framework reduces the dependence of flood simulation on dense, continuous hydrological gauge observations and provides a feasible technical approach for data-scarce regions.

Several limitations remain and should be addressed in future work:

(1) Hydraulic simulation accuracy is highly sensitive to terrain-data quality [43]. The hydraulic model in this study was constructed using available DEM and river cross-section data. Conventional DEMs generally represent the water surface and surrounding terrain but cannot accurately resolve channel morphology. Although measured cross-sections improve channel representation, they are usually sparse and cannot fully capture spatial variations in channel form. Future studies could incorporate higher-resolution terrain products, airborne LiDAR, unmanned aerial vehicle observations, and bathymetric surveys to improve geometric inputs to the hydraulic model.

(2) The SAR acquisition time limited the strength of the inundation constraint. Only one SAR image from the flood recession stage was available, rather than multiple images

covering the rising stage or flood peak. The observed inundation boundary therefore mainly represented in-channel flow conditions, reducing the sensitivity of IoU-based optimization to changes in Manning's roughness. Future studies should incorporate multitemporal SAR imagery covering the rising, peak, and recession stages to provide stronger spatial constraints throughout the complete flood evolution.

Among 399 distinct evaluated parameter combinations in the available PSO search records, 86 distinct objective-function values were each shared by two or more combinations. These values were identical at the stored numerical precision, without additional rounding. The discrete, raster-based calculation of IoU can contribute to these ties because different parameter combinations may produce unchanged binary inundation masks or the same intersection-to-union ratio. These results indicate that the single-date inundation constraint does not ensure unique identification of the six Manning's roughness parameters. The estimated parameters should therefore be interpreted as a fitted parameter set conditional on the adopted model and observations; their uncertainty and its propagation to simulation outputs require further assessment.

(3) Future work could combine river water levels retrieved from the Surface Water and Ocean Topography (SWOT) satellite with SAR-derived inundation extent to construct a joint point-and-area remote-sensing constraint. Such integration is expected to further reduce parameter equifinality and improve the robustness of Manning's roughness inversion.

(4) The downstream normal-depth boundary was specified using a fixed energy slope. The sensitivity of the inverted Manning's roughness parameters and validation metrics to this slope was not quantified. Consequently, the reported parameter estimates and model performance are conditional on the adopted downstream boundary setting. Future work will assess their sensitivity to plausible variations in the downstream energy slope.

Author Contributions: Conceptualization, S.W. and Z.P.; methodology, S.W., Z.P., J.F. and W.J.; software, S.W.; validation, S.W., D.C. and J.F.; formal analysis, S.W.; investigation, S.W., D.C. and Y.Z.; resources, D.C.; data curation, D.C.; writing—original draft preparation, S.W.; writing—review and editing, Z.P., D.C. and J.F.; visualization, S.W.; supervision, Z.P.; project administration, Z.P.; funding acquisition, Z.P. All authors have read and agreed to the published version of the manuscript.

Funding: This research was funded by Beijing Natural Science Foundation-Fengtai Joint Innovation Fund, grant number L241046, and the National Natural Science Foundation of China, grant number 42301450.

Data Availability Statement: The data are not publicly available due to confidentiality and privacy restrictions.

Acknowledgments: This work was supported by Beijing Natural Science Foundation-Fengtai Joint Innovation Fund under Grant No. L241046 (Research on key technologies of communication-navigation-remote sensing monitoring and early warning for extreme flood disasters) and the National Natural Science Foundation of China, grant number 42301450.

Conflicts of Interest: The authors declare no conflicts of interest.

References

1. Zotou, I.; Bellos, V.; Tsihrintzis, V.A. Calibration Framework for Complex 2D Hydrodynamic Models: Use of Satellite-Derived Flood Extent and Water Depth Data, and Evaluation with Various Performance Metrics. *Adv. Water Resour.* **2025**, *204*, 105066. [CrossRef]
2. Gomes, M.N., Jr.; Castro, M.D.A.R.A.; Sanchez, M.H.; Rápalo, L.M.C.; Giacomoni, M.H.; De Paiva, R.C.D.; Bates, P. Spatio-Temporal Performance of 2d Local Inertial Hydrodynamic Models for Urban Drainage and Dam-Break Applications. *J. Hydrol.* **2025**, *665*, 134661. [CrossRef]
3. Liu, Z.; Merwade, V.; Jafarzadegan, K. Investigating the Role of Model Structure and Surface Roughness in Generating Flood Inundation Extents Using One- and Two-dimensional Hydraulic Models. *J. Flood Risk Manag.* **2019**, *12*, e12347. [CrossRef]

4. Metcheka Kengne, I.G.; Delmas, V.; Soulaïmani, A. Calibration of Manning's Roughness Coefficients for Shallow-Water Flows on Complex Bathymetries Using Optimization Algorithms and Surrogate Neural Network Models. *Comput. Fluids* **2026**, *304*, 106884. [CrossRef]
5. Rad, H.R.; Ebrahimian, H.; Liaghat, A.; Omid, M.; Khalaji, F.; Arani, M.S. Integrating Image Processing and Machine Learning for Phase Specific Estimation of Manning Roughness Coefficient in Furrow Irrigation. *Sci. Rep.* **2025**, *15*, 37062. [CrossRef]
6. Lavoie, B.; Mahdi, T.-F. Manning's Roughness Coefficient Determination in Laboratory Experiments Using 2D Modeling and Automatic Calibration. *La Houille Blanche* **2020**, *106*, 22–33. [CrossRef]
7. Attari, M.; Hosseini, S.M. A Simple Innovative Method for Calibration of Manning's Roughness Coefficient in Rivers Using a Similarity Concept. *J. Hydrol.* **2019**, *575*, 810–823. [CrossRef]
8. Hajikandi, H.; Hatami, M. Assessment of Manning's Resistance Coefficient in Compound Channels. *J. Water Sci. Res.* **2010**, *2*, 9–20.
9. Arcement, G.J.; Schneider, V.R. *Guide for Selecting Manning's Roughness Coefficients for Natural Channels and Flood Plains*; U.S. Geological Survey Water-Supply Paper 2339; U.S. Government Printing Office: Washington, DC, USA, 1989.
10. Wibowo, H.; Suripin; Kodoatie, R.; Isdiyana. Comparing the Calculation Method of the Manning Roughness Coefficient in Open Channels. *Int. J. Eng. Res. Technol.* **2015**, *4*, 1278–1285.
11. Vrugt, J.A.; Gupta, H.V.; Bastidas, L.A.; Bouten, W.; Sorooshian, S. Effective and Efficient Algorithm for Multiobjective Optimization of Hydrologic Models. *Water Resour. Res.* **2003**, *39*, 2002WR001746. [CrossRef]
12. Ayvaz, M.T. A Linked Simulation–Optimization Model for Simultaneously Estimating the Manning's Surface Roughness Values and Their Parameter Structures in Shallow Water Flows. *J. Hydrol.* **2013**, *500*, 183–199. [CrossRef]
13. Drisya, J.; Sathish Kumar, D. Automated Calibration of a Two-Dimensional Overland Flow Model by Estimating Manning's Roughness Coefficient Using Genetic Algorithm. *J. Hydroinform.* **2018**, *20*, 440–456. [CrossRef]
14. Yang, F.; Wu, J.; Zhang, Y.; Zhu, S.; Liu, G.; Chen, G.; Wu, S.; Fan, Z. Improved Method for Identifying Manning's Roughness Coefficients in Plain Looped River Network Area. *Eng. Appl. Comput. Fluid Mech.* **2021**, *15*, 94–110. [CrossRef]
15. Teng, J.; Jakeman, A.J.; Vaze, J.; Croke, B.F.W.; Dutta, D.; Kim, S. Flood Inundation Modelling: A Review of Methods, Recent Advances and Uncertainty Analysis. *Environ. Model. Softw.* **2017**, *90*, 201–216. [CrossRef]
16. Beven, K.; Freer, J. Equifinality, Data Assimilation, and Uncertainty Estimation in Mechanistic Modelling of Complex Environmental Systems Using the GLUE Methodology. *J. Hydrol.* **2001**, *249*, 11–29. [CrossRef]
17. Aronica, G.; Hankin, B.; Beven, K. Uncertainty and Equifinality in Calibrating Distributed Roughness Coefficients in a Flood Propagation Model with Limited Data. *Adv. Water Resour.* **1998**, *22*, 349–365. [CrossRef]
18. Travert, J.-P.; Boyaval, S.; Goeury, C.; Bacchi, V.; Zaoui, F. Evaluation of Performance Measures for Comparing Flood Models With Satellite Observations. *Water Resour. Res.* **2025**, *61*, e2024WR038506. [CrossRef]
19. Giustarini, L.; Hostache, R.; Matgen, P.; Schumann, G.J.-P.; Bates, P.D.; Mason, D.C. A Change Detection Approach to Flood Mapping in Urban Areas Using TerraSAR-X. *IEEE Trans. Geosci. Remote Sens.* **2013**, *51*, 2417–2430. [CrossRef]
20. Bioresita, F.; Puissant, A.; Stumpf, A.; Malet, J.-P. A Method for Automatic and Rapid Mapping of Water Surfaces from Sentinel-1 Imagery. *Remote Sens.* **2018**, *10*, 217. [CrossRef]
21. Zhou, Y.; Liu, H.; Ma, F.; Pan, Z.; Zhang, F. A Sidelobe-Aware Small Ship Detection Network for Synthetic Aperture Radar Imagery. *IEEE Trans. Geosci. Remote Sens.* **2023**, *61*, 5205516. [CrossRef]
22. Pulvirenti, L.; Squicciarino, G.; Cenci, L.; Ferraris, L.; Virelli, M.; Candela, L.; Puca, S. Continuous Flood Monitoring Using On-Demand SAR Data Acquired with Different Geometries: Methodology and Test on COSMO-SkyMed Images. *ISPRS J. Photogramm. Remote Sens.* **2025**, *225*, 382–401. [CrossRef]
23. Zhang, X.; Chan, N.W.; Pan, B.; Ge, X.; Yang, H. Mapping Flood by the Object-Based Method Using Backscattering Coefficient and Interference Coherence of Sentinel-1 Time Series. *Sci. Total Environ.* **2021**, *794*, 148388. [CrossRef]
24. Hostache, R.; Chini, M.; Giustarini, L.; Neal, J.; Kavetski, D.; Wood, M.; Corato, G.; Pelich, R.; Matgen, P. Near-Real-Time Assimilation of SAR-Derived Flood Maps for Improving Flood Forecasts. *Water Resour. Res.* **2018**, *54*, 5516–5535. [CrossRef]
25. Hawker, L.; Neal, J.; Savage, J.; Kirkpatrick, T.; Lord, R.; Zylberberg, Y.; Groeger, A.; Thuy, T.D.; Fox, S.; Agyemang, F.; et al. Assessing LISFLOOD-FP with the next-Generation Digital Elevation Model FABDEM Using Household Survey and Remote Sensing Data in the Central Highlands of Vietnam. *Nat. Hazards Earth Syst. Sci.* **2024**, *24*, 539–566. [CrossRef]
26. Guo, G.; Yin, J.; Yuan, X.; Zhu, Z.; Guan, M.; Yu, D.; Wright, N. Validation of Urban Surface Water Flood Modeling with Multisource Data: Two Case Studies in Baoji and Linyi Cities, China. *Int. J. Disaster Risk Sci.* **2025**, *16*, 832–842. [CrossRef]
27. Sadeh, Y.; Cohen, H.; Maman, S.; Blumberg, D.G. Evaluation of Manning's *n* Roughness Coefficient in Arid Environments by Using SAR Backscatter. *Remote Sens.* **2018**, *10*, 1505. [CrossRef]
28. Wood, M.; Hostache, R.; Neal, J.; Wagener, T.; Giustarini, L.; Chini, M.; Corato, G.; Matgen, P.; Bates, P. Calibration of Channel Depth and Friction Parameters in the LISFLOOD-FP Hydraulic Model Using Medium-Resolution SAR Data and Identifiability Techniques. *Hydrol. Earth Syst. Sci.* **2016**, *20*, 4983–4997. [CrossRef]

29. Gobeyn, S.; Van Wesemael, A.; Neal, J.; Lievens, H.; Eerdenbrugh, K.V.; De Vleeschouwer, N.; Vernieuwe, H.; Schumann, G.J.-P.; Di Baldassarre, G.; Baets, B.D.; et al. Impact of the Timing of a SAR Image Acquisition on the Calibration of a Flood Inundation Model. *Adv. Water Resour.* **2017**, *100*, 126–138. [CrossRef]
30. Shahverdi, K.; Talebmorad, H. Automating HEC-RAS and Linking with Particle Swarm Optimizer to Calibrate Manning's Roughness Coefficient. *Water Resour. Manag.* **2023**, *37*, 975–993. [CrossRef]
31. Amani, K.; Hosseini, S.M. Enhancing Residual Flood Risk Assessment through Response Capacity Quantification: Case Study of the Sefidroud River, Iran. *Int. J. Disaster Risk Reduct.* **2026**, *134*, 106019. [CrossRef]
32. Belay, H.; Melesse, A.M.; Tegegne, G.; Kassaye, S.M. Flood Inundation Mapping Using the Google Earth Engine and HEC-RAS Under Land Use/Land Cover and Climate Changes in the Gumara Watershed, Upper Blue Nile Basin, Ethiopia. *Remote Sens.* **2025**, *17*, 1283. [CrossRef]
33. Larnier, K.; Garambois, P.; Emery, C.; Pujol, L.; Monnier, J.; Gal, L.; Paris, A.; Yesou, H.; Ledauphin, T.; Calmant, S. Estimating Channel Parameters and Discharge at River Network Scale Using Hydrological-Hydraulic Models, SWOT and Multi-Satellite Data. *Water Resour. Res.* **2025**, *61*, e2024WR038455. [CrossRef]
34. Amitrano, D.; Di Martino, G.; Iodice, A.; Riccio, D.; Ruello, G. Unsupervised Rapid Flood Mapping Using Sentinel-1 GRD SAR Images. *IEEE Trans. Geosci. Remote Sens.* **2018**, *56*, 3290–3299. [CrossRef]
35. Li, Z.; Demir, I. MultiRS Flood Mapper: A Google Earth Engine Application for Water Extent Mapping with Multimodal Remote Sensing and Quantile-Based Postprocessing. *Environ. Model. Softw.* **2024**, *176*, 106022. [CrossRef]
36. Li, Z.; Demir, I. U-Net-Based Semantic Classification for Flood Extent Extraction Using SAR Imagery and GEE Platform: A Case Study for 2019 Central US Flooding. *Sci. Total Environ.* **2023**, *869*, 161757. [CrossRef]
37. Chen, L.; Cai, X.; Li, Z.; Xing, J.; Ai, J. Where Is My Attention? An Explainable AI Exploration in Water Detection from SAR Imagery. *Int. J. Appl. Earth Obs. Geoinf.* **2024**, *130*, 103878. [CrossRef]
38. Manjusree, P.; Prasanna Kumar, L.; Bhatt, C.M.; Rao, G.S.; Bhanumurthy, V. Optimization of Threshold Ranges for Rapid Flood Inundation Mapping by Evaluating Backscatter Profiles of High Incidence Angle SAR Images. *Int. J. Disaster Risk Sci.* **2012**, *3*, 113–122. [CrossRef]
39. Guo, M.; Li, J.; Sheng, C.; Xu, J.; Wu, L. A Review of Wetland Remote Sensing. *Sensors* **2017**, *17*, 777. [CrossRef]
40. Li, X.; Takeuchi, W. Land Surface Water Coverage Estimation with PALSAR and AMSR-E for Large Scale Flooding Detection. *Terr. Atmos. Ocean. Sci.* **2016**, *27*, 473. [CrossRef]
41. Oliveira, E.R.; Disperati, L.; Alves, F.L. MINDED-FBA: An Automatic Remote Sensing Tool for the Estimation of Flooded and Burned Areas. *Remote Sens.* **2023**, *15*, 724. [CrossRef]
42. Zhai, M.; Shen, H.; Cao, Q.; Ding, X.; Xin, M. Water Body Extraction Methods for SAR Images Fusing Sentinel-1 Dual-Polarized Water Index and Random Forest. *Sensors* **2025**, *25*, 4868. [CrossRef]
43. Hamidi, E.; Nazari, B.; Moftakhari, H.; Moradkhani, H. Enhancing Compound Flood Simulation Accuracy and Efficiency in Urbanized Coastal Areas Using Hybrid Meshes and Modified Digital Elevation Model. *Sustain. Cities Soc.* **2025**, *121*, 106184. [CrossRef]

Disclaimer/Publisher's Note: The statements, opinions and data contained in all publications are solely those of the individual author(s) and contributor(s) and not of MDPI and/or the editor(s). MDPI and/or the editor(s) disclaim responsibility for any injury to people or property resulting from any ideas, methods, instructions or products referred to in the content.